Numerical Investigation on Unsteady Pressure Oscillation of Gas‑Solid Two‑Phase Turbulent Flow

YANG Yong, *ZANG Wenwen*, *HAN Xingsi**, *MAO Junkui*

College of Energy and Power Engineering, Nanjing University of Aeronautics and Astronautics, Nanjing 210016, P.R.China

Abstract: Relevant to thermoacoustic combustion instability in engines, the pressure oscillations in gas‑solid two‑phase turbulent flow have long been a topic of great concerns. To understand the pressure oscillation characteristics in gas‑solid two‑phase flow, three-dimensional unsteady numerical calculations are conducted for typical two‑phase gas‑solid backstep flow using the combined self-adaptive turbulence eddy simulation (SATES) and discrete phase model (DPM) method. The accuracy and reliability of the numerical method is firstly validated by comparisons with the experimental data. Then, the unsteady pressure signal of the two‑phase gas‑solid flow is compared with that of the pure gas phase flow, and it is found that with the addition of solid particles, the dominant frequency of pressure oscillation is slightly changed, and the oscillation amplitude significantly decreases. Finally, the effects of diameter and mass fraction of solid particles on the pressure oscillation are investigated. It is found that with increasing the solid particle diameter, the amplitude of pressure oscillation firstly decreases and then increases, and the amplitude exhibits the smallest with the diameter of 10 μm; with increasing the mass fraction of solid particle, the pressure oscillation amplitude shows a decreasing trend. The results demonstrate that the properties of solid particles in two‑phase flow have a small impact on the dominant frequency of pressure oscillation, while a significant impact on the oscillation amplitude.

Key words: pressure oscillation; gas‑solid two‑phase backstep turbulent flow; self-adaptive turbulence eddy simulation (SATES); discrete phase model (DPM); frequency‑spectra characteristics

CLC number: V211.6   **Document code:** A   **Article ID:** 1005-1120(2024)03-0311-14

0 Introduction

The rapid evolution of missile technology has led to an escalation in the performance demands placed on propulsion systems. In the development of solid rocket engines, primary trends have emerged, focusing on high loading, substantial thrust, and increased aspect ratios. Nevertheless, in their pursuit of high performance, these engines frequently manifest unstable combustion[1-2], marked by periodic pressure oscillations. This periodic pressure oscillations can lead to more severe thrust oscillations, affecting the normal operation of engines. In certain instances, this instability can lead to irreversible structural damage to the combustion chamber, diminishing reliability and contributing to engine failures, with the potential for catastrophic accidents[3]. Previous research on the periodic pressure oscillations within solid rocket engines mainly focused on pure gas flow. On the contrary, contemporary solid rocket engines predominantly employ the combustion of aluminum powder to augment propellant energy and elevate specific impulse, thus rendering the internal flow field of the engine a classic example of gas‑solid two‑phase flow[4]. Within this context, comprehending the attributes of solid particles in the engine's two‑phase flow holds considerable importance for delving further into the unstable combustion phenomena observed in high‑performance solid

rocket engines primarily governed by gas-solid two-phase flow.

During the initial phases of research, both domestic and international scholars predominantly relied on experimental methods to explore the impact of particles on fluid dynamics in two-phase flow fields, specifically through the damping effect. Temkin et al.[5] were the first to propose a formula for calculating particle-induced damping in acoustic waves in 1966. They introduced a dimensionless number, the Stokes number (Stk), to describe the acoustic damping effect of particles. Culick[6] made a series of modifications to this formula in 1974. Blomshield et al.[7] explored the damping characteristics of propellants containing ultrafine aluminum powder. They conducted experiments with four different metallized propellants, varying the sizes and relative concentrations of coarse and ultrafine aluminum. Experimental results showed that the presence of ultrafine aluminum powder in the engine did not significantly dampen vibrations. Numerical simulation is also a crucial tool for studying two-phase flow fields. Cai et al.[8] utilized the Euler-Lagrange method to conduct numerical simulations of the interaction between two-phase flow and vortex-induced acoustic oscillations in solid rocket engines. Their research indicated that acoustic oscillations can readily transfer energy from periodic motion to turbulence, leading to an increase in turbulence intensity and an early transition from laminar to turbulent flow. Conversely, turbulence-induced vortices have a tendency to dampen the vortical motion generated by acoustic waves. Chaturvedi et al.[9] performed numerical simulations of solid rocket engines with embedded cavities. They studied the influence of particle properties in the propellant on slag accumulation in the nozzle. The calculations revealed that when particle diameter is small, nozzle slag accumulation is minimal. Daniel[10] introduced a transient compressible flow model considering particle phase effects and conducted simulation calculations on a cylindrical rocket engine. The calculation results indicated that particle injection velocity and the initial particle size significantly influence the two-phase flow. Fontes et al.[11] conducted two-dimen-

sional numerical analyses of rocket particle jet flow using both Euler-Euler and Euler-Lagrange methods. The computational results demonstrated that both methods perform well in solving particle velocity and distribution in high-speed compressible flows within rocket plumes. Yu et al.[12-13] employed particle trajectory models and a two-fluid model successively to numerically simulate gas-solid two-phase flow in JPL nozzles. Their research delved into the influence of solid particle properties on the gas-solid two-phase flow within nozzle flow field. Sun et al.[14-15] utilized the pulse decay method for two-dimensional calculations of two-phase flow inside nozzles. They explored the key factors affecting the damping characteristics of solid rocket engine nozzles. By varying parameters such as gas temperature and pressure, they investigated the variation patterns of nozzle damping in solid rocket engines. Furthermore, the computational results provided insights for improving cold flow experiments.

Based on a summary and analysis of past research, it has been observed that the current studies on gas-solid two-phase flow primarily rely on the Reynolds-averaged Navier-Stokes (RANS) method. Moreover, many of these studies simplify two-phase flow in engines to two-dimensional flow. However, concerning the pressure oscillations characteristics in gas-solid two-phase flow, the flow inherently exhibits unsteady pulsations. Traditional RANS methods struggle to accurately predict unsteady pulsations. Therefore, there is a pressing need for three-dimensional, unsteady, and high-precision numerical simulations to investigate the impact of solid particle properties on the pressure oscillations characteristics in gas-solid two-phase flow. This research aims to unveil the influence patterns of solid particles on pressure oscillations frequency and amplitude, along with an analysis of the underlying physical mechanisms.

This paper focuses on the study of the common backstep gas-solid two-phase flow in rocket engines. It employs the newly developed self-adaptive turbulence eddy simulation (SATES) method in conjunction with the multiphase flow discrete phase model (DPM) for three-dimensional, unsteady, and high-

precision numerical simulations. The research aims to investigate the influence of particle properties on flow pressure oscillations characteristics, laying the groundwork for further exploration of thermoacoustic-coupled unstable combustion in gas-solid two-phase flow within rocket engines. Notably, this paper marks the first application of the SATES method in high-precision numerical simulations of gas-solid two-phase flow. The paper begins with a brief introduction to the numerical simulation methods used. It then validates the developed SATES-DPM method's accuracy and reliability in calculating the flow field of backstep gas-solid two-phase flow, using experimental data as a reference. Finally, the paper computes and compares the pressure oscillations characteristics between backstep gas-solid two-phase flow and pure gas-phase flow. Furthermore, it conducts a detailed analysis of the impact patterns and characteristics of particle diameter and mass fraction on the dominant frequency and amplitude of flow field pressure oscillations.

1 Numerical Computational Methods

1.1 Baseline k-ω turbulence model

For unsteady turbulent flow, direct solving of the Navier-Stokes equations, known as direct numerical simulation (DNS) currently demands significant computational resources. Hence, researchers have proposed a series of turbulence models to model and solve turbulent problems in different dimensions as per their requirements. Apart from DNS, common turbulence models can generally be classified into three categories: RANS, large eddy simulation (LES), and various forms of hybrid methods (RANS/LES). Among these, RANS methods still dominate in complex engineering computations.

The baseline k-ω model (referred to as BSL k-ω model) is a two-equation eddy-viscosity RANS turbulence model introduced by Menter[16], which builds upon earlier turbulence models. Essentially, the BSL k-ω model is a hybrid of the k-ε and k-ω models. This model employs the k-ω method in the near-wall region and the k-ε method in the free tur-

bulent zone, combining the strengths of both models. Its governing equations are as follows

$$\frac{\mathrm{D}(\rho k)}{\mathrm{D}t} = P_k - \beta^* \rho k \omega + \frac{\partial}{\partial x_j}\left[\left(\mu + \sigma_k \mu_t \frac{\partial k}{\partial x_j}\right)\right] \quad (1)$$

$$\frac{\mathrm{D}(\rho \omega)}{\mathrm{D}t} = \frac{\gamma \omega}{k} P_k - \beta \rho \omega^2 + \frac{\partial}{\partial x_j}\left[(\mu + \sigma_{\omega 1} \mu_t) \frac{\partial \omega}{\partial x_j}\right] + $$

$$2(1 - F_1)\rho \sigma_{\omega 2} \frac{1}{\omega} \frac{\partial k}{\partial x_j} \frac{\partial \omega}{\partial x_j} \quad (2)$$

$$F_1 = \tanh(\phi^4) \quad (3)$$

where F_1 represents the blending function, assuming that ϕ_1 signifies any constant from the original k-ω model; ϕ_2 any constant within the expression after transforming to the k-ω model, and ϕ the corresponding constant in the new model. These respective constants can be uniformly expressed as

$$\phi = F_1 \phi_1 + (1 - F_1)\phi_2 \quad (4)$$

Based on the aforementioned model, some of the primary model constants in this model are given in Table 1.

Table 1 Some main model constants in BSL k-ω model

β_1	β_2	β^*	σ_{k1}	σ_{k2}	$\sigma_{\omega 1}$	$\sigma_{\omega 2}$
0.075	0.082 8	0.09	0.5	1.0	0.5	0.856

1.2 Self-adaptive turbulence eddy simulation method

The RANS method models turbulence by averaging it over all scales, making it challenging to accurately describe the turbulent fluctuation evolution characteristics in unsteady flows. Consequently, its computational accuracy tends to be lower in flows with intense unsteady turbulence. The LES method directly resolves the primary large-scale turbulent structures and can effectively capture the unsteady nature of turbulence. Nonetheless, in high-Reynolds-number flows, particularly in close proximity to walls, LES can prove to be computationally demanding. To strike a balance between computational accuracy and efficiency, researchers have proposed various RANS-LES methods. In recent years, unified modeling turbulence simulation methods have garnered significant attention, and among them is one known as "very-large eddy simulation (VLES)". VLES is a variant of LES that aims to

provide a compromise between the benefits of LES and the computational cost of RANS in simulating unsteady turbulent flows. The SATES framework used in this study is an extension of the VLES method developed and extensively validated by Han et al[17-19]. Extensive numerical verification work has shown that, even on very coarse computational grids, the VLES method developed by Han et al. can still directly resolve over 90% of the turbulent kinetic energy. Additionally, rigorous theoretical derivations have also demonstrated that the new VLES method developed by Han et al is entirely equivalent to LES when the grid is sufficiently refined[17-23]. This means that Han et al's VLES model is fundamentally different from Pope's defined VLES model. To avoid confusion between the two, this study refers to it as the SATES method.

The SATES model is based on the low Mach number Newtonian fluid assumption and solves the filtered governing equations. In this context, the residual turbulent stress needs to be modeled, and it is modeled and solved based on the underlying BSL $k\text{-}\omega$ model. This is achieved by introducing a resolution control function F_r to re-model the turbulent viscosity coefficient μ_t, as shown in Eq.(5), to make it scale with the grid resolution-related residual scales.

$$\mu_t = F_r \rho \frac{k}{\omega} \quad (5)$$

The resolution control function F_r, as expressed in Eq.(6), is the core of the SATES model in this study.

$$F_r = \min\left(1.0, \left[\frac{1.0 - \exp(-\beta L_c/L_k)}{1.0 - \exp(-\beta L_i/L_k)}\right]^n\right) \quad (6)$$

where β and n are empirical constants in the model, with values of 0.002 and 2, respectively; L_i, L_c, and L_k represent three characteristic length scales in turbulent calculations: the turbulent integral length scale, the filtering length scale, and the smallest Kolmogorov length scale. These three length scales correspond to the characteristic length scales in the traditional RANS, LES, and DNS methods, respectively. Therefore, in essence, the SATES method integrates aspects of these three traditional turbulence simulation methods. The expressions for the three length scales are as follows

$$L_c = C_x (\Delta_x \Delta_y \Delta_z)^{\frac{1}{3}} \quad (7)$$

$$L_i = k^{\frac{3}{2}}/(\beta^* k\omega) \quad (8)$$

$$L_k = \nu^{\frac{3}{4}}/(\beta^* k\omega)^{\frac{1}{4}} \quad (9)$$

where C_x is a model parameter determined through correlation with basic LES and RANS models[17]. In this study, the model constant used is $C_x = 0.61$.

1.3 Discrete phase model (DPM)

The DPM follows the Euler-Lagrange framework. The fluid phase is treated as the continuous phase, and its governing equations are solved using the Eulerian method. The discrete phase, on the other hand, is computed using the Lagrange method, allowing for the calculation of the motion of a large number of solid particles within the flow field. Momentum, mass, and energy exchanges can occur between the discrete phase and the fluid phase.

The DPM model is primarily used when the discrete phase concentration is relatively small. This method does not consider the impact of particles on fluid motion, making it suitable for cases where the volume fraction of particles in the total volume is relatively small.

Considering that the solid particle density in this study is much greater than that of the gas phase, and it represents a dilute phase, with both mass and volume fractions being very low, the following assumptions can be made:

(1) Only consider the effect of particles on the flow field, neglecting other particle interactions.

(2) Assume that spherical particles with the same diameter are injected into the flow field.

(3) Neglect the influence of gravity, Magnus force, Saffman force, etc., and consider only drag force effects.

Under these assumptions, the equations governing particle motion are as follows

$$\frac{\mathrm{d}x_p}{\mathrm{d}t} = u_p \quad (10)$$

$$\frac{\mathrm{d}u_p}{\mathrm{d}t} = \frac{F_D}{1/6\pi d_p^3 \rho_p} \quad (11)$$

$$F_D = \frac{1}{2} C_D \rho_f A_p (u_f - u_p) |u_f - u_p| \quad (12)$$

where x_p represents the particle position; t the time; u_p the particle velocity; u_f the fluid velocity; τ_p the particle relaxation time; d_p the particle diameter; F_D the drag force per unit mass of the particle; A_p the particle surface area, and C_D the drag coefficient, typically related to the particle Reynolds number; ρ_f and ρ_p are the respective densities of the fluid and particle, respectively. The particle Reynolds number is defined as

$$Re = \frac{\rho_f d_p (u_f - u_p)}{\mu} \quad (13)$$

$$C_D = a_1 + \frac{a_2}{Re_p} + \frac{a_3}{Re_p^2} \quad (14)$$

where the coefficient values a_1, a_2 and a_3 can be referenced from relevant research, such as the work of Morsi et al[24].

In gas-solid two-phase flow, the Stokes number (Stk) is commonly used as a dimensionless criterion to describe the motion characteristics of particles in the fluid. It is defined as the ratio of particle inertia to diffusion effects and can be expressed as shown in Eqs.(15—17). A smaller Stokes number indicates less particle inertia, making it easier for particles to follow fluid motion, and diffusion effects become more significant. Conversely, a larger Stokes number indicates greater particle inertia, reducing the particles' ability to follow the fluid motion.

$$\tau_f = L/u_f \quad (15)$$

$$\tau_p = \frac{d_p^2 \rho_p}{18\mu} \quad (16)$$

$$Stk = \frac{\tau_p}{\tau_f} = \frac{\rho_p d_p^2 u_f}{18L\mu} \quad (17)$$

where τ_f is the residence time; τ_p the particle relaxation time; ρ_p and d_p are the particle density and diameter, respectively; u_f the fluid velocity; μ the dynamic viscosity of the fluid, and L the characteristic length.

2 Computational Method Validation

This study uses the classic experimental data from Fessler et al.[25] for the validation of the numer-ical methods. In their research, experiments were conducted using copper spheres with a diameter of 70 μm and a mass fraction of 3%. The experimental system provided uniform fluid velocity at the inlet and introduced particle loading. Starting from the inlet, the fluid passed through a 5.2 m long channel to reach the test section, allowing for adequate flow development and providing sufficient time for particles to reach equilibrium with the channel flow.

2.1 Geometry and mesh

In the experiment from Ref.[25], the expansion ratio of the backstep was 5/3, and the height of the step H was 26.7 mm. In this study, three-dimensional SATES model is used for unsteady numerical simulations. In the simulations, the development length L_2 in the downstream direction of the step is set to twice the experimental size, i.e., $L_2 = 34H$, to ensure that turbulence can fully develop. The rest of the geometric dimensions remain consistent with the experiment, as depicted in Fig.1.
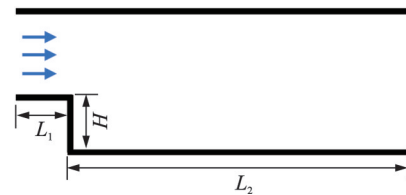

Fig.1   Geometric diagram of backstep flow

The numerical computation domain has an inlet length of $L_1 = H$, and a development length of $L_2 = 34H$. The spanwise width of the calculated domain is $2H$. Before computation, the entire domain undergoes preprocessing, and structured grids are employed. Local refinement of the mesh is applied near the backstep, the walls, and around the shear layer. This study conducts a mesh sensitivity analysis using two sets of grids with cell counts of 1.5 million and 3 million, respectively. The results show consistent accuracy between the two sets of grids, and the grid with 3 million cells is chosen for numerical computations. The grid division in the computational domain is illustrated in Fig.2, with local refinement near the walls and shear layer.
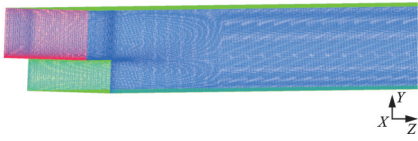
Fig.2   Computational grid of backstep flow

2.2   Numerical method validation

2.2.1   Boundary and computational settings

The study employs experimental data from Ref. [25] as a reference to validate the numerical computation method. The boundary conditions for numerical computation are determined based on the experimental conditions. In the experiment, the reference condition has a Reynolds number based on the step height of 18 400. To ensure that the Reynolds number in numerical computation matches the experiment, the inlet mainstream velocity U_0 is set to 10.5 m/s. Considering the full development of the flow, a synthetic pulsatile turbulent flow is introduced into the computational domain based on the $\frac{1}{7}$ th power velocity distribution pattern. For boundary conditions, no-slip conditions are applied to the upper and lower surfaces of the walls, a pressure outlet boundary condition is used at the outlet, and periodic boundary conditions are applied in the spanwise direction.

Simulations are initially performed on the pure gas-phase flow without the introduction of particles. Once the flow field reaches a stable state, particles are subsequently introduced under conditions consistent with those specified in the literature.

The numerical calculations are performed using pressure-based transient solver to solve the equations. The pressure-velocity coupling is achieved using the semi-implicit method for pressure-linked equations-consistent (SIMPLEC) algorithm, with second order upwind scheme for the pressure term, bounded central differencing scheme for the convective term, and second order upwind scheme for the turbulent scalar equation. Time discretization is achieved using bounded second order implicit scheme. The time step is set to 1e−4 to keep the CFL number at 1.0.

2.2.2   Validation of numerical results

Initially, numerical simulations are performed to validate the flow of pure gas-phase over the backstep. Fig.3 shows the axial time-averaged velocity streamline plot for the pure gas-phase flow field. From the results, it can be observed that the recirculation length of the backstep obtained from numerical calculations is approximately 7.2H, which is in good agreement with the experimental measurement result of 7.4H. Additionally, the classical diagonal vortex in the backstep flow field is accurately captured in the numerical simulation.
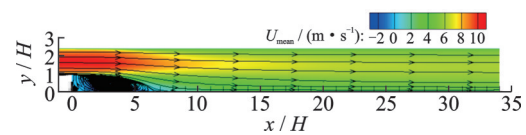

Fig.3   Contour of predicted mean axial velocity and streamline for the pure gas flow

Next, solid particles are introduced into the stable gas-phase flow field. The particles have a diameter of 70 μm, a density of 8 800 kg/m³, a dimensionless Stokes number of 10.2, and a mass fraction of 3%. The calculated values of gas-phase streamwise-averaged velocities at $x/H=2$, 5, 7, 9, and 12 cross-sections are compared with experimental data from the literature and the LES results from this study, as shown in Fig.4. From Fig.4, it can be observed that the calculated streamwise velocities in the flow field agree well with the experimental data. At several locations, the predictions from the SATES method even outperform the results obtained using the traditional LES approach.

Red line: SATES results; blue line: LES results
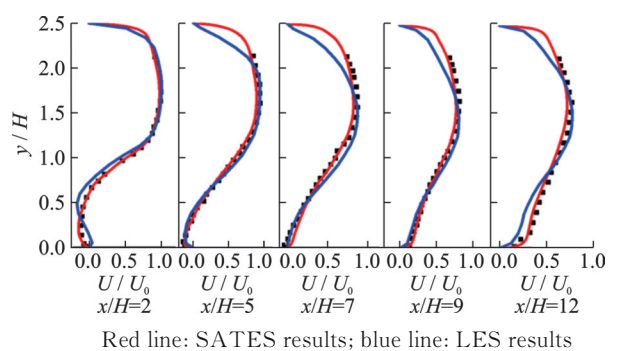
Fig.4   Comparisons of mean axial velocity of gas phase in gas-solid two-phase flow at different locations

Fig.5 presents the numerical results of the particle streamwise-averaged velocities at $x/H=2$, 5, 7, 9, and 12 cross-sections in the gas-solid two-

phase flow field. From it, it is evident that the numerical results obtained using the SATES method agree well with the experimental data and, overall, slightly outperform the traditional LES results.


Red line: SATES results; blue line: LES results
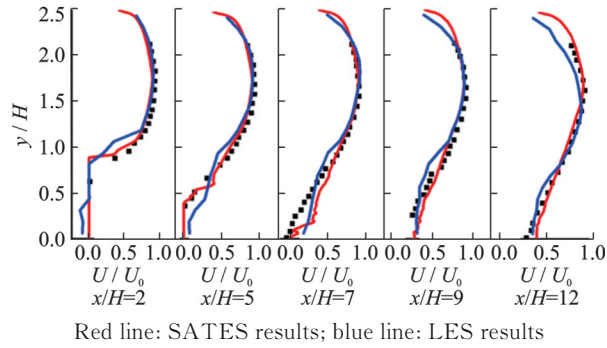
Fig.5   Comparisons of mean axial velocity of solid phase in gas-solid two-phase flow at different locations

These results indicate that in the context of gas-solid two-phase flow over a backstep, the proposed approach, combining the SATES model with DPM, provides accurate predictions. Both the gas-phase and particle-phase results are in good agreement with experimental data and are superior to the traditional LES approach.

In order to further compare the dependence of the calculation results of SATES, LES and RANS (SST k-ω) on the grid resolution, the above three methods are used to calculate the pure gas phase backstep turbulent flow with an expansion ratio of 2/1 and a Reynold number of 15 000. Other calculation settings remain the same as above. Fig.6 shows the comparison between the experimental data[26] and the calculation results of different calculation methods on three sets of grids with 1.5 million, 3 million and 10 million cells, respectively.

As can be seen from Fig.6, when the number of grids is 1.5 million, the calculation accuracy of LES is even worse than that of SST k-ω because the grid resolution cannot meet the requirements of LES. In contrast, the calculation accuracy of SATES is much higher than that of LES and better than that of SST k-ω in less number grids. When the number of grids is increased to 3 million, the calculation accuracy of LES is obviously improved, and that of SST k-ω is slightly improved. But SATES is still the best performer of the three. When the number of grids is increased to 10 mil-

lion, the calculation accuracy of SST k-ω is almost unchanged, and that of LES is slightly improved. The calculation accuracy of LES and SATES is almost the same under such fine mesh, both of them maintain a good agreement with the experimental data, and their performance is better than SST k-ω. According to the comparison of the accuracy of the three methods under different grid resolutions, the performance of SATES is better than that of LES and SST k-ω under less grid number, and no worse than that of LES under sufficient grid resolution.

Red line: SATES results; blue line: LES results; green line: SST k-ω results; black dot: experimental data
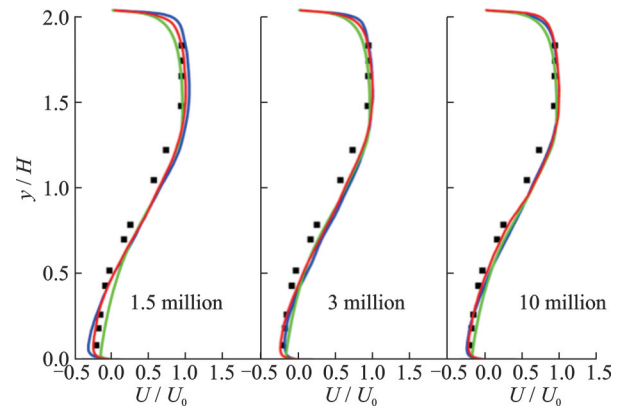
Fig.6   Comparison of streamwise velocity at x/H=5 calculated by three methods under different grid numbers with experimental data

Fig.7 shows the three-dimensional vortex structure in the shear layer behind the step captured by SATES for grid with a number of 3 million cells.
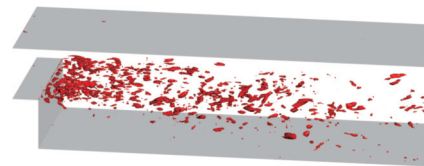
Fig.7 Q=1.7e−6 iso-surface calculated by SATES when the number of cells is 3 million

3   Pressure Oscillation Characteristics

In the previous section, the reliability of the SATES model combined with DPM used in this paper for simulating gas-solid two-phase flow, is confirmed through comparative analysis. To examine

pressure oscillation characteristics in the backstep flow field, we explore the impact of solid particles on pressure oscillation, using the same geometric and flow conditions as in the previous section. Following that, a comprehensive investigation into how varying particle diameters and mass fractions influence the dominant frequency and amplitude of pressure oscillation in gas-solid two-phase flow over the backstep is carried out.

3.1 Pressure oscillation characteristics in gas-solid two-phase flow field

In this section, the Reynolds number used for the calculations is $Re=92\ 000$, corresponding to an inlet velocity of 52.5 m/s for the gas phase. The boundary conditions and computational settings are consistent with those used in the previous verification case.

Initially, numerical simulations are conducted for the pure gas phase flow without solid particles. After achieving flow field stability, the static pressure at four locations within the shear layer is monitored and recorded. The locations of these monitoring points are provided in Table 2. The mean axial velocity streamline plot of the pure gas phase flow is depicted in Fig.8, illustrating that the computational results are consistent with the established findings from previous studies on the early stages of backstep flow.

Table 2   Location of the monitoring points

| Index	1	2	3	4
Location	$(0.5H,H)$	$(1.5H,H)$	$(5.5H,H)$	$(6H,H)$
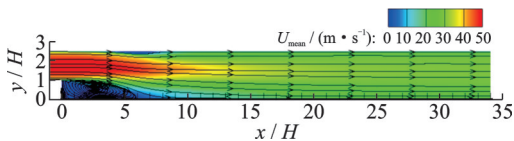
Fig.8   Contours of mean axial velocity and streamline for the pure gas flow at $Re=92\ 000$

The obtained time-series pressure data are subjected to fast Fourier transform (FFT) to obtain the pressure oscillation spectra at each location. The results of these calculations are presented in Fig.9, where the vertical axis represents the dimensionless amplitude of pressure oscillation. From Fig.9, it is

evident that there is a pronounced broad peak phenomenon within the flow field, and there exists a dominant frequency corresponding to the maximum oscillation amplitude at the shear layer location. The results in Fig.9 show that the dominant frequency gradually decreases along the downstream direction while the dimensionless pressure oscillation amplitude decreases. At point 1, the dominant frequency is approximately 1 382 Hz, with the dimensionless pressure oscillation amplitude of around 0.61. As the flow progresses to point 2, the dominant frequency decreases to around 800 Hz, with the dimensionless pressure oscillation amplitude decreasing to about 0.47. Further downstream at points 3 and 4, the dominant frequency decreases significantly to around 100 Hz, and the dimensionless pressure oscillation amplitude further reduces to approximately 0.1. Near the sudden expansion of the backstep, a high velocity gradient is present in the shear layer, and this gradient gradually decreases as it moves downstream. This characteristic can be observed in the mean axial velocity contour shown in Fig.9. In general, a substantial region of instability exists within the recirculation zone of the backstep flow, and the trends in the variation of dominant frequency and amplitude of instability along the downstream direction are closely linked to changes in velocity gradient.

The variations in the dominant frequency at different locations reveal that in proximity to the backstep, the flow instability characteristics are predominantly influenced by the shear layer instability generated within a short distance downstream of the step. This results in a dominant frequency of around 1 382 Hz, corresponding to a Strouhal number (St) of 0.703. As these small vortices enter the central region of the recirculation zone, the dominant frequency of oscillation gradually decreases. Ultimately, within the reattachment region, they evolve into larger vortices that govern the oscillations at a frequency corresponding to $St \approx 0.1$. As a result, the Strouhal number associated with the primary oscillations in each section gradually decreases along the downstream direction and tends to approach a con-

stant value in the later regions.

After the pure gas-phase flow field has stabilized, numerical simulations of the gas-solid two-phase flow are carried out. Solid particles with a diameter of 70 μm, a density of 8 800 kg/m³, and a

mass fraction of 3％ are introduced into the flow field, while keeping all other boundary conditions unchanged. FFT is applied to pressure monitoring data of the same sample size, resulting in spectra for each downstream position as shown in Fig.10.
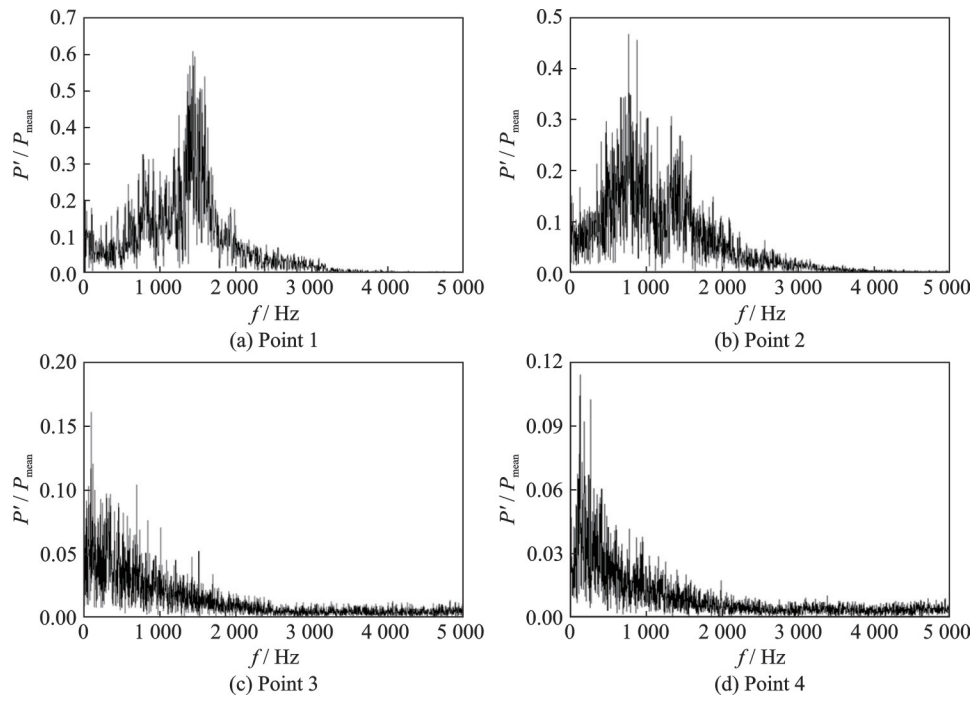
Fig.9   Pressure oscillation spectra of pure gas flow at different flow positions
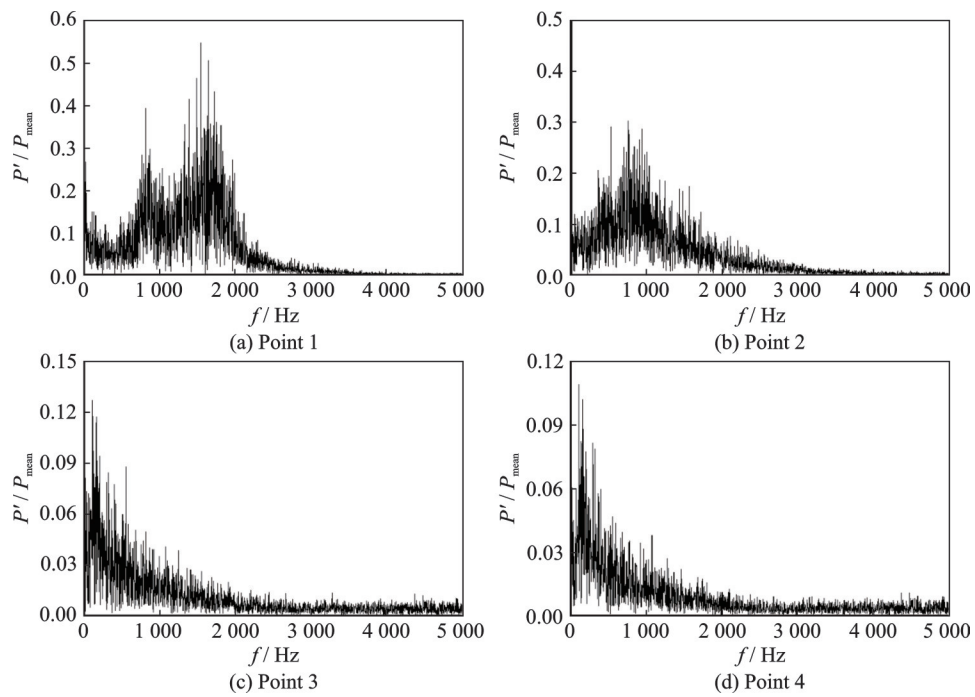

Fig.10   Pressure oscillation spectra of gas phase in two-phase flow at different flow positions

Compared to the results of the pure gas-phase flow field, the introduction of particles does not sig-

nificantly alter the macroscopic characteristics of the unstable region. Near the step location, the instabili-

ty is still primarily dominated by small vortices formed shortly downstream of the step. As these small vortices enter into the central part of the recirculation zone, the dominant oscillation frequency gradually decreases. However, there are slight changes in the dominant frequency at each monitoring point location, and the dimensionless amplitude of pressure oscillation is notably reduced compared to the pure gas-phase flow field. This indicates that the addition of particles introduces a damping effect on the momentum exchange within the flow field, making the transfer and exchange of momentum more complex. The interaction between particles and the gas phase leads to the generation of more vortices that excite unstable oscillations, resulting in a more pronounced broad-peak phenomenon. At the same time, this damping effect reduces the amplitude of pressure oscillations.

3.2　Influence of particle diameter on the oscillation characteristics

To further investigate the influence of particle parameter variation on the oscillation characteristics in the two-phase flow over the backstep, a series of high-precision numerical simulations are conducted by varying particle diameters. This section aims to find the relationship between particle diameter and the dominant frequency and amplitude of flow field oscillations.

After achieving stability in the pure gas-phase flow field, solid particles with diameters of 1, 10, 40, and 70 μm are individually introduced while maintaining a particle density of 8 800 kg/m^3 and a mass fraction of 3%. The other boundary conditions and computational settings remain the same. Pressure monitoring is conducted at the positions specified in Table 2, and the data collected, of the same sample size, undergo FFT analysis. It provides the dominant oscillation frequency and dimensionless pressure amplitude at each downstream location, and the summarized results are presented in Fig.11.

From Fig.11, it is evident that with an increase in particle diameter, the dominant frequency of pressure oscillations at various monitoring locations re-

(a) Amplitude of pressure oscillation under different particle diameters

(b) Frequency of pressure oscillation under particle diameters
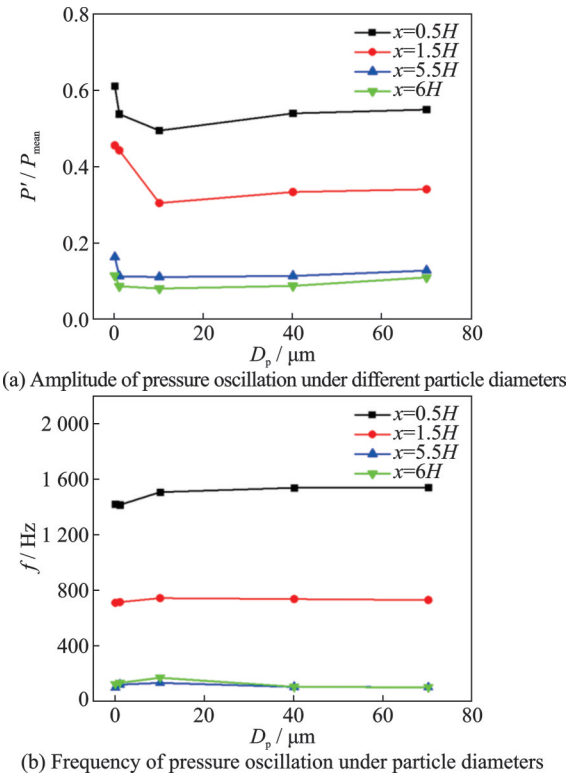
Fig.11　Comparisons of amplitude and frequency characteristics under different particle diameters

mains relatively consistent. However, the dimensionless pressure amplitude undergoes substantial variations, displaying an initial decrease followed by an increase. When the particle diameter in the flow field reaches D_p=10 μm, the dominant frequency of oscillations in the flow field shows a noticeable increase only at the x=0.5H position, with minimal changes observed at other locations. Within the same range of particle diameter variations, there is a significant decrease in the dimensionless pressure amplitude, which is most pronounced at the x=0.5H and x=1.5H positions. However, when the particle diameter increases further from D_p=10 μm, although the dimensionless amplitude increases somewhat, the magnitude of this change is not substantial, and the dominant frequency tends to stabilize. Therefore, within a certain range, D_p=10 μm can be considered the "optimal diameter" with the lowest dimensionless pressure amplitude. At this point, the corresponding Stokes number is approximately 1.

The particle distribution for different particle diameters is illustrated in Fig.12. From Fig.12, it can

be observed that the "particle-free zone" in the flow field gradually increases with an increase in particle diameter. When the particle diameter is 1 μm, their distribution in the flow field is more uniform, with more particles being entrained into the recirculation region by the gas. This suggests that at a diameter of 1 μm, the particles exhibit better entrainment with the flow. As the particle diameter increases, the Stokes number also increases, and the influence of inertia on particle motion becomes more noticeable. Consequently, the particles show reduced entrainment with the flow, resulting in fewer particles following the gas into the recirculation region.
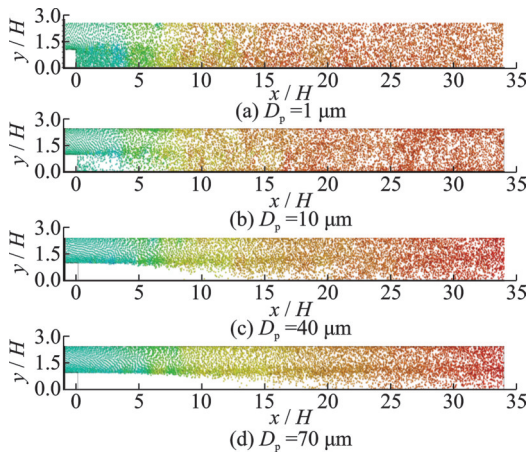
Fig.12   Particle distribution for different cases with particle diameters (pressure coloring)

3.3   Influence of particle mass fraction on the oscillation characteristics

To further investigate the influence of particle parameter variation on the oscillation characteristics in the two-phase flow over the backstep, a series of high-precision numerical simulations are conducted by varying particle mass fraction. This aims to study the effect of particle mass fraction on the dominant frequency and amplitude of flow field oscillations. The physical model, computational methods, and boundary conditions remain unchanged. The gas-solid two-phase flow over the backstep is calculated for four different operating conditions with particle mass fractions of 6%, 12%, 21%, and 30%, respectively. The particle diameter for each case is held constant at 70 μm.

At monitoring points set in the flow behind the

step, flow field static pressure is monitored. The recorded time-series pressure oscillation data are then subjected to FFT analysis to obtain the corresponding dominant oscillation frequencies and dimensionless pressure oscillation amplitudes. The data collected is summarized and organized to obtain the amplitude and frequency characteristics of the flow field for different particle mass fractions, as shown in Fig.13.

(a) Amplitude of pressure oscillation under different particle mass fractions

(b) Frequency of pressure oscillation under different particle mass fractions
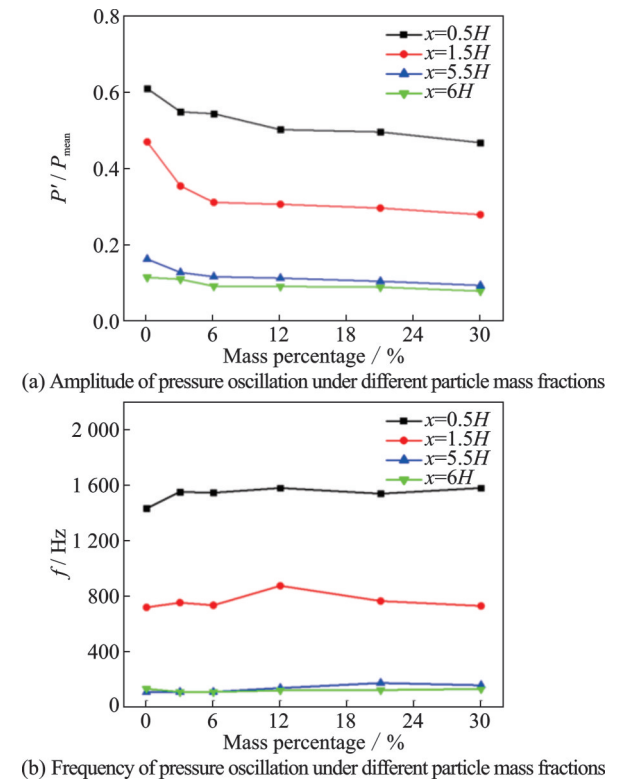
Fig.13   Comparisons of amplitude and frequency characteristics under different particle mass fractions

The results in Fig.13 show that as the particle mass fraction increases, the dimensionless amplitude of pressure oscillations at various monitoring points gradually decreases. This indicates that inertial particles have some inhibitory effect on pressure oscillations at monitoring points. This inhibitory effect becomes more pronounced as the particle mass fraction increases. The graph also shows that this inhibitory effect is more significant at points 1 and 2 than points 3 and 4. This suggests that under the same particle mass fraction, the introduction of particles has a more pronounced inhibitory effect on pressure oscillations in positions where oscillations

are originally stronger. When the particle mass fraction increases from 0 to 6%, the reduction in the dimensionless amplitude of pressure oscillations at all monitoring points is quite noticeable. However, when the particle mass fraction increases from 6% to 30%, within a relatively large range of mass fraction variations, the reduction in the dimensionless amplitude of pressure oscillations is minimal. This phenomenon indicates that increasing the particle mass fraction has a certain saturation effect on the inhibitory effect of pressure oscillations in the gas-solid two-phase flow field. Increasing the particle mass fraction cannot completely suppress the instability of the flow field. Analyzing the variations in dominant oscillation frequencies at different particle mass fractions, it is noticeable that the impact of particle mass fraction on the dominant frequency of pressure oscillations is relatively minor.

The distribution of particles in the flow field under different mass fractions is shown in Fig.14. From the figure, it can be observed that changes in particle mass fraction do not significantly affect the distribution characteristics of particles in the flow field. The size of the "particle-free zone" in flow field with different particle mass fractions is essentially the same. This phenomenon may be because the particle mass fraction does not directly appear in the expression for the Stokes number. Therefore,
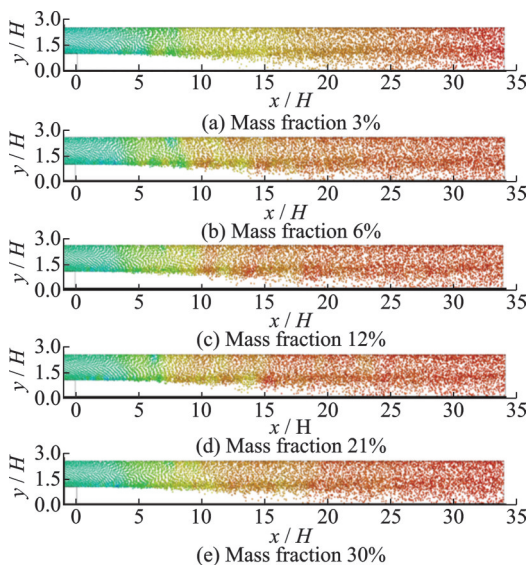

Fig.14   Particle distribution for different cases with different mass fractions (pressure coloring)

changes in mass fraction do not affect the magnitude of the particle Stokes number. Consequently, they do not significantly alter the entrainment of particles in the gas-solid two-phase flow.

4   Conclusions

The study employs an advanced SATES model combined with DPM to conduct high-precision numerical simulations of the gas-solid two-phase flow field over the backstep. Through a comparison of the numerical results with experimental data, the developed SATES-DPM method is validated to exhibit a high level of computational accuracy and reliability. Subsequently, the research delves into the unsteady pressure oscillation characteristics of the gas-solid two-phase flow field over the backstep and elucidated the influence of key particle parameters on the pressure oscillation characteristics. The main conclusions can be drawn from this study as follows.

(1) This study has provided validation for the newly developed coupled approach of SATES and DPM. It exhibits a high degree of computational precision in accurately predicting complex flow characteristics within gas-solid two-phase flow.

(2) In the pure gas-phase flow behind the step, there is a noticeable presence of pressure oscillations. After introducing solid particles into the flow field, the flow becomes more complex. The dominant frequency of oscillations in the flow field slightly decreases, and the dimensionless amplitude of pressure oscillations notably diminishes. The influence of particles in the flow field is equivalent to introducing a damping effect on the gas phase.

(3) The variation in particle diameter in the two-phase flow behind the step has a minimal impact on the dominant frequency of pressure oscillations but significantly affects the dimensionless amplitude. Within the scope of the study, as the diameter increases, the dimensionless amplitude initially decreases and then increases. With a particle diameter of $D_p = 10$ μm, all monitoring points within the flow display the lowest dimensionless amplitude. Smaller particle diameters correspond to better particle entrainment in the flow.

（4）The variation in particle mass fraction in the two-phase flow behind the step also has minimal impact on the dominant frequency of pressure oscillations but significantly affects the dimensionless amplitude. Within the scope of the study, as the particle mass fraction increases, the dimensionless amplitude consistently decreases. However, the reduction in dimensionless amplitude is more significant when the mass fraction is below 6%. It becomes relatively smaller when the mass fraction exceeds 6%. Additionally, the change in particle mass fraction does not significantly alter its distribution characteristics in the flow field.

References

［1］ SUN Weishen. Solid rocket engine unstable combustion［M］. Beijing: Beijing University of Technology Press,1988. (in Chinese)

［2］ DOWLING A P, MAHMOUDI Y. Combustion noise［J］. Proceedings of the Combustion Institute, 2015, 35(1): 65-100.

［3］ JOO S, KWAK S, LEE J, et al. Thermoacoustic instability and flame transfer function in a lean direct injection model gas turbine combustor［J］. Aerospace Science and Technology, 2021, 116: 106872.

［4］ PANG Aimin, LI Xiaoping. Innovation and development laws of solid propellant technology［J］. Chinese Journal of Energetic Material, 2015, 23(1): 3-6. (in Chinese)

［5］ TEMKIN S, DOBBINS R A. Attenuation and dispersion of sound by particulate-relaxation processes［J］. The Journal of the Acoustical Society of America, 1966,40(2):317-324.

［6］ CULICK F E C. T-burner testing of metalized solid propel-lants［R］.［S.l.］:［s.n.］, 1974.

［7］ BLOMSHIELD F, NGUYEN S, MATHEKE H, et al. Acoustic particle damping of propellants containing ultra-fine aluminum［C］//Proceedings of AIAA/ASME/SAE/ASEE Joint Propulsion Conference & Exihibit.［S.l.］: AIAA, 2006.

［8］ CAI Weidong, MA Fuhua, YANG Vigor. Two-phase vorticoacoustic flow interactions in solid-propellant rocket motors［J］. Journal of Propulsion & Power, 2003, 19(3): 385-396.

［9］ CHATURVEDI A K, KUMAR S, CHAKABORTY D. Slag prediction in submerged rocket nozzle through two-phase CFD simulations［J］. Defence Science Journal, 2015,65(2): 99-106.

［10］ DANIEL E. Eulerian approach for unsteady two-phase solid rocket flows with aluminum particles［J］. Journal of Propulsion & Power, 2015, 16(2): 309-317.

［11］ FONTES D H, MIKKELSEN D, KINZEL M P. Analysis of rocket jet particulate using Euler-Lagrange and Euler-Euler approaches［C］//Proceedings of AIAA Scitech 2020 Forum.［S.l.］: AIAA, 2020.

［12］ YU Yong, LIU Shuyan, ZHANG Shijun, et al. Numerical simulation of gas-solid two-phase flow in solid rocket engine nozzle［J］. Journal of Aerospace Power, 2009(4): 931-937. (in Chinese)

［13］ YU Yong, ZHANG Xia, CHEN Wei. Simulation of supersonic gas-solid two-phase flow using a two-fluid model［J］. Journal of Aerospace Power, 2010,25(4): 800-807. (in Chinese)

［14］ SUN Bingbing, LI Junwei, SU Wanxing, et al. Numerical simulation of damping characteristics in solid rocket engine nozzle［J］. Journal of Aerospace Power, 2016, 31(9): 2290-2297. (in Chinese)

［15］ SUN Bingbing, LI Junwei, SU Wanxing, et al. Study on the influence of temperature and pressure on damping in rocket engine nozzles［J］. Propulsion Technology, 2016, 37(5): 844-851. (in Chinese)

［16］ MENTER F R. Two-equation eddy-viscosity turbulence models for engineering applications［J］. AIAA Journal, 1994, 32(8): 1598-1606.

［17］ HAN X S, KRAJNOVIĆ S. An efficient very large eddy simulation model for simulation of turbulent flow［J］. International Journal for Numerical Methods in Fluids, 2013, 71(11): 1341-1360.

［18］ HAN X S, KRAJNOVIĆ S. Validation of a novel very large eddy simulation method for simulation of turbulent separated flow［J］. International Journal for Numerical Methods in Fluids, 2013, 73(5): 436-461.

［19］ HAN X, KRAJNOVIĆ S. Very-large-eddy simulation based on k-ω model［J］. AIAA Journal, 2015, 53(4): 1103-1108.

［20］ XIA Z, HAN X, MAO J. Assessment and validation of very-large-eddy simulation turbulence modeling for strongly swirling turbulent flow［J］. AIAA Journal, 2020, 58(1): 148-163.

［21］ XIA Z, CHENG Z, HAN X, et al. VLES turbulence modelling for separated flow simulation with OpenFOAM［J］. Journal of Wind Engineering and Industrial Aerodynamics, 2020, 198: 104077.

［22］ WANG T, XUAN Y, HAN X. Investigation on hybrid thermal features of aero-engines from combustor to turbine［J］. International Journal of Heat and Mass Transfer, 2023, 200: 123559.

［23］ MIN Y, WU W, ZHANG H, et al. Self-adaptive tur-

bulence eddy simulation of flow control for drag reduction around a square cylinder with an upstream rod[J]. European Journal of Mechanics—B /Fluids, 2023, 100: 185-201.

[24] MORSI S A, ALEXANDER A J. An investigation of particle trajectories in two-phase flow systems[J]. Journal of Fluid Mechanics, 1972, 55(2): 193-208.

[25] FESSLER J R, EATON J K. Turbulence modification by particles in a backward-facing step flow[J]. Journal of Fluid Mechanics, 1999, 394: 97-117.

[26] FUREBY C. Large eddy simulation of rearward-facing step flow[J]. AIAA Journal, 1999, 37(11): 1401-1410.

Authors   Mr. **YANG Yong** received his B.S. degree from Nanjing University of Aeronautics and Astronautics (NUAA) in 2021. And he is now pursuing the M.S. degree at NUAA. His research interests focus on numerical simulation of engine combustion and fluid dynamics.

Prof. **HAN Xingsi** received his B.S. and Ph.D. degrees from University of Science and Technology of China (USTC) in 2000 and 2009, respectively. Subsequently, he served as a postdoctoral researcher at University of Paris VI, France, from 2009 to 2010, followed by another postdoctoral position at Chalmers University of Technology in Sweden from 2011 to 2013. From 2013 to 2016, he worked as a research assistant at Imperial College London in the United Kingdom. Since 2016, he has worked in NUAA, where he holds the positions of a professor and a doctoral supervisor. His research interests primarily focus on advanced numerical simulations of complex thermal-fluid phenomena in aviation propulsion systems, encompassing aspects such as turbulent flow, heat transfer, cooling, and combustion.

Author contributions   Mr. **YANG Yong** completed the organization of the entire text, the calculation of the cases, and the writing of the content. Ms. **ZANG Wenwen** completed some of the data processing work. Prof. **HAN Xingsi** provided the ideas and the model foundation. Prof. **MAO Junkui** made many important revisions to the draft. All authors commented on the manuscript draft and approved the submission.

Competing interests   The authors declare no competing interests.

(Production Editor: WANG Jing)

气固两相湍流非定常压力脉动特性数值模拟研究

阳　勇,臧雯雯,韩省思,毛军逵

(南京航空航天大学能源与动力学院,南京 210016,中国)

摘要: 与发动机振荡燃烧相关的气固两相流中的压力脉动现象长期以来备受关注。为了解发动机气固两相流动中的非定常压力脉动特性,以典型的后台阶气固两相流动为研究对象,使用发展的自适应湍流模拟(Self-adaptive turbulence eddy simulation, SATES)和离散相模型(Discrete phase model, DPM)相结合的方法,对两相流场进行了三维非定常高精度数值计算。以实验数据作为参考验证了计算方法的精度和可靠性。通过将两相流场的压力脉动信号与纯气相流场进行对比,发现加入颗粒后流场压力脉动主导频率略有变化,无量纲压力脉动幅值明显减小;进一步研究了固体颗粒直径和质量分数对脉动特性的影响规律,发现随着颗粒直径变大,流场振幅先减小后增大。颗粒直径为 10 μm 时,振幅最小;随着质量分数的增大,流场振幅呈现出下降趋势。研究表明气固两相流中颗粒的参数变化对振荡主频影响较小,对脉动振幅影响显著。

关键词: 压力脉动;后台阶气固两相流;自适应湍流模拟;离散相模型;频谱特性